UC San Diego
UC San Diego Previously Published Works

Title

Effects of digital fringe projection operational parameters on detecting powder bed defects in additive manufacturing

Permalink

https://escholarship.org/uc/item/7w05s0xd

Authors

O'Dowd, Niall M
Wachtor, Adam J
Todd, Michael D

Publication Date

2021-12-01

DOI

10.1016/j.addma.2021.102454

Peer reviewed

EFFECTS OF DIGITAL FRINGE PROJECTION OPERATIONAL PARAMETERS ON DETECTING POWDER BED DEFECTS IN ADDITIVE MANUFACTURING

Niall M. O'Dowd[1]**, Adam J. Wachtor**[2]**, and Michael D. Todd**[3]

[1,3]Department of Structural Engineering, University of California San Diego
[1,2,3]Engineering Institute, Los Alamos National Laboratory
[1]nmodowd@eng.ucsd.edu, [2]ajw@lanl.gov, [3]mdtodd@eng.ucsd.edu (corresponding author)

Abstract. Additive manufacturing is a technology transforming traditional production timelines. Specifically, metal additive manufacturing (MAM) has been increasingly adopted by a variety of industries, not only to prototype, but also to fulfill full production scale applications with much lower lead times. Like any maturing manufacturing technology, developments in verifying and validating processes are necessary to support continuous growth. Due to the complex nature of MAM, part quality and repeatability remain integral challenges that inhibit further adoption of MAM for critical component production. In this study, we present data taken from a developing in-process monitoring system designed to measure and detect powder bed defects (PBDs) in powder bed fusion MAM systems using surface height maps created with structured light illumination. We showcase the feasibility of the monitoring technique for in-process implementation by detecting streak PBDs with varying severities (height, width) created in a lab environment. We present results of powder bed measurements for varying experimental parameters of the structured light system such as illumination angle, illumination pattern, and number of illuminations. We also present an expression used to determine experimental height noise based on input parameters for PBD detection based on the instrument transfer function of the structured light monitoring system for arbitrary pixel intensity noise contributions. With the results of PBD detection across across multiple experimental measurement parameters, we provide a best practices approach to in-process implementation of the monitoring system in powder bed fusion manufacturing.

1 Introduction

Metal additive manufacturing (MAM) is an advanced manufacturing technique witnessing accelerating adoption in various fields with exponential market growth [1]. Within the past decade, MAM has significantly penetrated the aerospace industry [2], largely due to the opportunities to fabricate parts with substantial weight savings [3], reduced production time [4], and design freedom only made possible by the additive process [5]. Medical device design and production has also been greatly impacted by MAM, especially the implant industry, where batches of customized "one-off" implants can be manufactured simultaneously. MAM is making the transition from early prototyping applications to a wide range of production applications at scale [6].

A driving factor of double-digit MAM market growth is the improvement to build quality, funded by significant research initiatives from by multiple US agencies, such as the Department of Energy [7], Department of Defense [8], and National Institute of Standards and Technology [9]. These very

agencies, as well as many reports from academic institutions [10, 11], and even major industry players, have expressed that the primary challenges preventing further industry adoption of MAM involve assessment of part quality and repeatability. These challenges arise as MAM relies on many moving parts and mechanisms responsible for part fabrication, e.g. material delivery, thermal gradients, and rapid material solidification. MAM quality control is an active area of research [12], especially as traditional quality control techniques often operate in a destructive *ex-situ* paradigm, which has been shown to be inadequate for MAM processes, due to inherent uniqueness of same-batch parts, and high post-inspection cost. Traditional non-destructive evaluation techniques are also ill-suited for MAM, as most have limited access to crucial internal part surfaces, or present difficulties qualifying part metrology. Such is the case for powder bed fusion (PBF), a common method of MAM, where a series of metallic powder layers are raked across a build chamber using a recoater blade, and a laser or electron beam is used to melt subsequent layers to create a three-dimensional part, layer-by-layer.

Powder bed defects (PBDs), i.e. defects occurring during the powder recoating process, are a main contributor of defects in as-built parts from PBF processes. PBDs include striations, depressions, and clumping, and can lead to detrimental part defects such as keyhole porosity formation, lack-of-fusion (LoF) pores, and even damage to the recoater blade [13–19]. Keyhole and LoF porosity have been observed to occur in regions of powder non-uniformity, where the melting process occurs with a volumetric energy density (VED) that is too high, or too little, respectively. Non-uniformity in powder layer thickness contributes to irregular VED — a function of laser parameters and powder layer thickness that has been observed to be related to the inception of cascading keyholing and LoF defects [20, 21]. Irregular powder coating also can produce unintended out-of-plane geometrical features, resulting in chipping or skipping of the recoater blade, consequently observed to create PBDs in subsequent layers due to inadequate raking of powder across the build chamber [22]. A common denominator of the causes of PBDs is the localized height of the powder layer, making the full field powder thickness measurement a crucial feature of *in-situ* monitoring, and the focus of this study.

Previous literature on the development of *in-situ* powder monitoring systems may be grouped generally into two categories: systems which measure features *related to* powder height, and systems which measure powder height *directly*. Many studies in the first category detail camera systems which use images to infer powder height irregularities with detectors such as pixel thresholding, or neural networks. It may be argued that these systems do not measure powder height, as pixel intensity is not a function of geometry, but rather use detectors that trigger when shadows are cast due to non-uniform powder height. While systems which use image processing to infer powder height show promising PBD detection results [22–24], these systems do not provide dimensional measurements, quantified uncertainty, or features related to VED which is coupled to the physics of defect formation. The monitoring system presented in this study belongs in the second category mentioned, designed to provide dimensional measurements of PBDs with quantified uncertainty.

Several techniques have been explored to provide full field *in-situ* powder height measurements. Development of a contact imager has been published by [16, 17], both using a linear imaging array (taken from an office copy machine) attached to the recoater blade inside a PBF machine. Estimations of full field height maps of the powder coat were made by a Laplacian-based focus measure operator, which was able to classify layer heights based on particle location deviations from the focus plane of the imager. Both authors reported very high resolution measurements, though expressed challenges

pertaining to uncontrollable recoater blade movement inside most commercially available printers.

Laser-based raster scanning height measurement techniques, such as high speed spectral domain optical coherence tomography [21] and in-line coherent imaging [25], have also been shown to provide powder height measurement in an *in-situ* paradigm. Although intrinsically single-point measurement systems, sampling resolution has been implemented for *in-situ* monitoring at sample rates above 50 kHz, contributing to scan speeds up to 1 m/s. Published works [21, 25] report maximum axial (height) and spatial (limited by beam diameter) resolutions as 7μm and 25μm, respectively, with axial repeatability as high as 0.47 μm. Coherent imaging systems remain an active area of research due to their high repeatability, though limitations in cost and relatively coarse spatial resolution may prevent the technique from wide-scale adoption.

A low-cost alternative to coherent imaging is non-coherent imaging, specifically digital fringe projection (DFP) — a structured light measurement technique. Success cases have been published detailing systems which use a projector and camera(s) to estimate height maps of PBDs during part fabrication. Proof-of-concept systems have been detailed in [26, 27] using single and stereo cameras in conjunction with a projector to measure the full field height of the powder bed to detect PBDs. Liu et. al produced two studies on *in-situ* powder measurement, and accurate calibration of such systems, showcasing spatial and axial measurement accuracy [13, 14]. While these publications provide results with excellent resolution and accuracy, the PBD measurements were not accompanied with a statistically quantified uncertainty model, or any indication of an exploration of optimal measurement parameters (such as illumination angle, effects of spatial filtering, fringe pattern selection, or number/fidelity of projection patterns).

In this study, detection of PBDs using a DFP system was investigated while employing an accompanying uncertainty model to execute a parametric study evaluating multiple measurement parameters. The effects of varying DFP operational parameters (illumination angle, number of projections, and fringe pitch) on detection of PBDs is reported and used to determine parameters best suited for *in-situ* PBD monitoring, and a best-practice approach to determine such parameters is outlined. DFP measurements were collected on intentionally created PBDs in a laboratory setup that mimicked powder distribution in PBF systems. The results presented herein contribute advances to both the optical engineering community by evaluating the performance of a novel operating method of DFP uncertainty quantification, and the MAM monitoring community by showcasing the use and effects of measurement parameters of PBD detection using a novel DFP system.

2 Methods and Approach

In order to explore the performance of the DFP measurements, lab procedures were developed to compare multiple operational parameters for the DFP system. This study presents data showcasing the impacts of PBD detection using DFP with a range of number of shifted projections (referred further as "bins N"), projector illumination angle θ, and spatial fringe pitch P. A water atomized stainless steel AISI 304 alloy powder (MilliporeSigma; catalog number GF02863841, batch 3110) reported to have a maximum particle size of $45\mu m$ was selected for use in all experiments. Lab conditions were designed to simulate the powder deposition process which occurs during each layer of a PBF build.

Several pieces of hardware were fabricated to study the detection capabilities, sensitivity, and
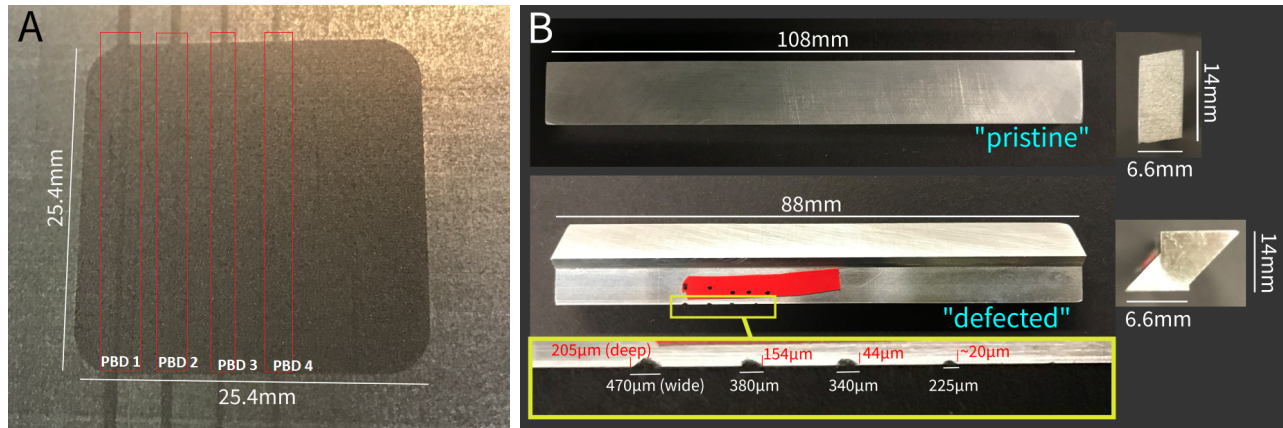
Figure 1: A) Photo of the experimental invesigation area with induced powder bed defects. B) Hardware used for powder distribution and defect creation.

noise structures of DFP height mapping. Figure 1A shows the aluminum tray that was fabricated with a filleted-square recess to allow for uniform powder coating to mimic the conditions of a PBF printer. The figure also shows a realization of intentional PBDs created using a modified recoater blade with four damage locations representative of the size and shape of PBDs which can occur in the PBF process. The "pristine" recoater blade was used to create a uniform powder bed to serve as the DFP reference surface, and the "defective" recoater blade was used to create realizations of raised-streak PBDs. The "defective" blade was fabricated with a set of four notches, increasing in size and width, and was used to create realizations of PBDs. Each realization of PBDs were made using the same "raking" motion to move powder across the aluminum tray, producing an intrinsically random, but consistent surface structure. A Keyence VHX-1000 height measurement microscope (Figure 2B) was used to estimate the characteristic height and width of the PBDs, for example, during the set of measurements further reported in Section 2.3, the PBD defect realization created by the "defective" blade produced four streak PBDs, of approximate heights of $150 - 180\mu m, 105 - 120\mu m, 45 - 75\mu m, 20 - 45\mu m$ for PBDs 1-4 shown in Figure 1A.

The prototype DFP monitoring system was comprised of a research projector, camera, and laptop for triggering and processing images. The projector is an EKB Technologies DPM-E4500MKII-OX On-Axis Focusable projector; the illumination optics are the Texas Instruments DLP® LightCrafter™ 4500 chipset and software package. This particular projector was selected for it's variable focus, and 0% offset projection optics to allow the possibility of altering throw distance and field-of view by adding concentric lenses. A Basler Ace acA4600 GigE camera was used to capture images of projected fringes. The camera position was kept constant at a viewing angle of approximately 60°, with the center of the front lens positioned at $x \approx 7$" and $z \approx 13.5$" (directions denoted in Figure 2A). Pixel pitch spacing in this study were approximately $50\mu m$. The output triggering functionality of the projector was used to trigger camera image acquisition. This allowed us to capture fringe images at uniform intervals to eliminate projector "draw lines" which occur without synchronization. A separate computer controlled the Keyence VHX-1000 used to verify certain dimensions of the PBDs. A photo of the experimental lab setup is shown in Figure 2B.
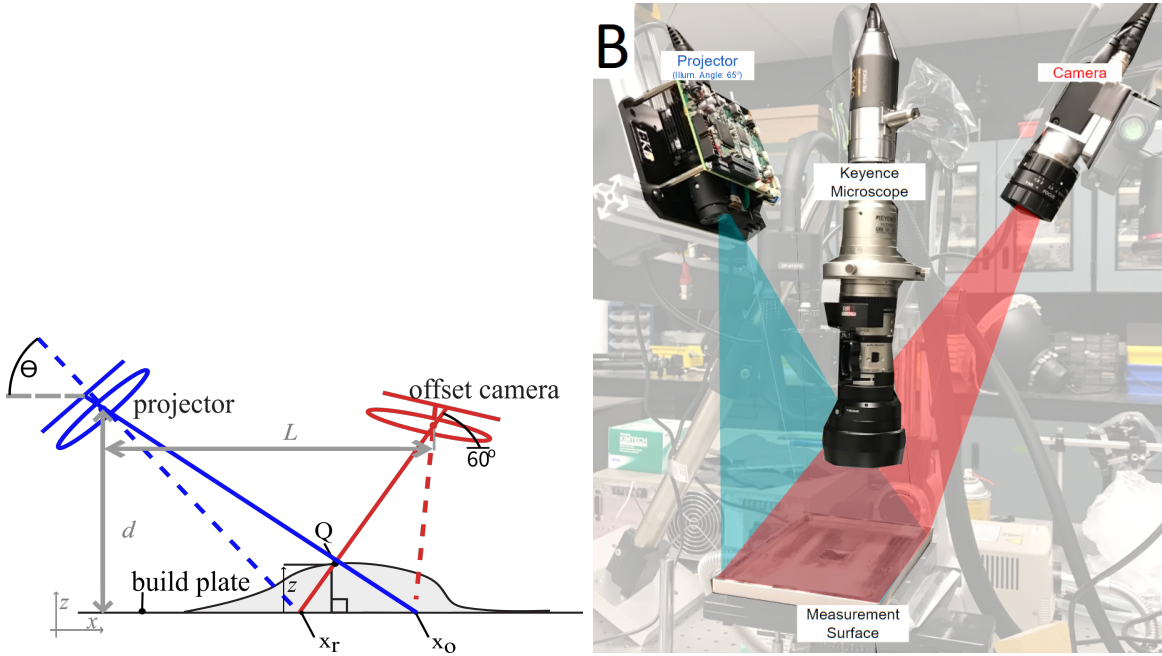
Figure 2: A) General two-dimensional schematic of the digital fringe projection measurement. B) Experimental digital fringe projection monitoring setup and the shape measurement Keyence microscope used to provide characterization of powder bed defects.

2.1 Overview of Digital Fringe Projection

Commonly, DFP height measurements are made by projecting patterns onto a flat reference plane (physical or mathematical, denoted further with subscript "r"), then placing an object onto the scene, and recording how the projected patterns deform from the object's shape (denoted further with "o"). Resultant calculations of the deformation of the fringe patterns produce a phase map, which is then converted to a height map through a calibration routine. During *in-situ* measurements inside a PBF machine, the reference surface can be taken as the bare base plate, or the base plate with a uniform initial powder coat. If DFP geometries are expected to stay constant, the reference phase map can be mathematically produced to allow differential height measurements independent of any height profile of the reference surface. Below, we outline the experimental process to produce a differential phase map, and the conversion to a differential height map.

A representative DFP experimental setup schematic and a photo of the lab experimental setup is shown in Figure 2. The projected patterns are often sinusoidally varying computer generated images, known as "fringes", with pixel intensity value f assigned according to:

$$f_i(x) = R[\cos(\frac{2\pi x}{P} + \delta_i) + 1], \tag{1}$$

where R is an interpolation function generated during a gamma calibration routine to increase the sinusoidal nature of the incident fringes (described in Section 2.2), P is the fringe pitch, and N phase-shifted images are generated and projected onto both reference and object with (equipartitioned) spatial shifts of $\delta_n = 2\pi n/N$, $n = 1...N$ (further referred to as "bins," where n is the projection index). Equation 1 creates a fringe pattern with varying intensity as a function of x, as it relates to Figure 2A.

The camera records images of the incident fringes on both reference and object surfaces, where the intensity $I_{(r,o)}$ of any fringe incident on a surface (either the reference r or object o) at any given

measurement point $x_{(r,o)}$ is given by [28] as:

$$I_{(r,o)} = A_{(r,o)} + B_{(r,o)} \cos\left(2\pi x_{(r,o)}/P\right), \tag{2}$$

where $A_{(r,o)}$ and $B_{(r,o)}$ are the background intensity due to projector bias (combined with ambient light intensity) and the projected fringe contrast, respectively, at the arbitrary point $x_{(r,o)}$. In order to recover differential information between object and reference phases, which is functionally related to the object height [29], the measurement point's "n-th" projection intensity in Equation 2 may be each written as:

$$I_{(r,o),n} = A_{(r,o),n} + B_{(r,o),n} \cos\left(\phi_{(r,o)} + \delta_n + \phi_c\right), \tag{3}$$

where $\phi_{(r,o)} = 2\pi x_{(r,o)}/P$ is the phase, ϕ_c accounts for the phase offset of the point in relation to the carrier phase (undeformed phase of the projected fringe pattern), and subscript "n" is the bin index. Once images are recorded of the projected fringes on the reference and object, phase $\phi_{r,o}$ (either on the reference or object), is found by:

$$\phi_{(r,o)} = \arctan\left(\frac{-\sum_{n=1}^{N} I_{(r,o),n} \sin \delta_n}{\sum_{n=1}^{N} I_{(r,o),n} \cos \delta_n}\right), \tag{4}$$

where it is assumed that nonlinear projector gamma issues (described thoroughly in [30–32]) are negligible or appropriately corrected/calibrated. In practice, Equation 4 produces a wrapped phase map where values are modulo 2π, due to the arctangent function $\epsilon\{-\pi, \pi\}$. While there is substantial research on best practices for phase unwrapping, the unwrapping process for our application is rather trivial do to the nominally planar geometry of the powder bed surface. Equation 4 represents a single phase map, which can be filtered to provide resolution of height-dependent features; this process is shown in Section 2.3. To continue to create a differential height measurement, the difference between phase of the object ϕ_o and reference ϕ_r surfaces is ultimately used. Continuing the derivation, the object-reference point's phase difference is given by:

$$\begin{aligned}
\phi &= \phi_o - \phi_r \\
&= \arctan\left(\frac{-\sum_{n=1}^{N} I_{o,n} \sin \delta_n}{\sum_{n=1}^{N} I_{o,n} \cos \delta_n}\right) - \arctan\left(\frac{-\sum_{n=1}^{N} I_{r,n} \sin \delta_n}{\sum_{n=1}^{N} I_{r,n} \cos \delta_n}\right) \\
&= \frac{2\pi (x_o - x_r)}{P}.
\end{aligned} \tag{5}$$

Geometrically, the height of a measurement point, z, from a reference point can be represented as a function of the geometries of the DFP experimental setup: L (scalar component of the projector-camera vector which is parallel to the reference plane), d (normal distance of the projector from the reference plane), and P (spatial fringe pitch on reference plane), and the scalar quantities x_r and x_o, seen in Figure 2. Many applications of the DFP method use a linearized phase-to-height measurement model, which assumes that the spacing between the projector and camera components L is much larger than the geometric distance between reference and object ray projections x_r and x_o, i.e. $L >> (x_o - x_r)$. Effectively, this assumption is valid for small height measurements, inclusive of all measurements taken in this study. This assumption provides the principal height measurement relationship of an arbitrary measurement point Q shown in Figure 2A (developed using similar triangles shown by the solid and

dashed ray traces, described in detail in [28]), z, given by:

$$z = \frac{d\left(x_o - x_r\right)}{L}.$$ (6)

Combining Equations 5 and 6, we can express z as a function of the measured differential phase ϕ and geometrical properties of the DFP system as:

$$z(\phi) = \frac{Pd\phi}{2\pi L}.$$ (7)

The variables P, d and L can prove difficult to measure accurately during experiment due to projector and camera housing blocking direct access to the illumination and imaging chips, respectively. However, because these variables remain constant during measurement, a calibration constant (found by a calibration routine explained in detail in [29, 33] and seen in Figure 4) replaces these quantities

$$z(\phi) = C\phi,$$ (8)

where $C = \frac{Pd}{2\pi L}$.

As mentioned, the goal of this article is to provide both qualitative and quantitative analyses of the effects of key parameters of the DFP on measurement of PBDs. Specific practices were developed to ensure a fair comparison of measurements across the parameter space explored, such as consistent phase-to-height conversion constants and fringe contrast across the four illumination angles for the absolute height measurements. The following subsections describe the experimental procedure for two types of DFP measurements.

2.2 Differential Height Measurements

Substantial portions of the data used for analysis in this paper are height maps of PBDs created through differential phase measurements, referred herein as differential height (DH) measurements. DH measurements reflect the operational measurement process intended for *in-situ* PBD monitoring. A high level summary of the measurement process for each illumination angle θ is as follows: projector gamma interpolation factors are obtained to generate gamma-corrected fringe projections, phase-to-height calibration constants are obtained by translating the stage in the z-direction while recording the resultant phase maps, new phase maps are made for the "pristine" and "defect" powder beds, and DH measurements are made by subtracting the reference phase map from the PBD phase map, then converted to height using the linearized calibration constant.

The illumination angle θ influences the phase-to-height relationship by altering geometric parameters d and L within equation 7 . To maintain an approximately consistent phase-to-height calibration constant C, the spatial fringe pitch P was altered. For example, to achieve a phase-to-height calibration constant of approximately 2.27 mm/ϕ at illumination angles $\{5, 25, 45, 65\}$ degrees, spatial fringe pitch P of approximately $\{1.1, 0.71, 0.41, 0.18\}$ mm were used for our projection geometry. Figure 3 shows an example of images of projected fringes within the measurement area with adjusted spatial fringe pitch P to accommodate different illumination angles θ.

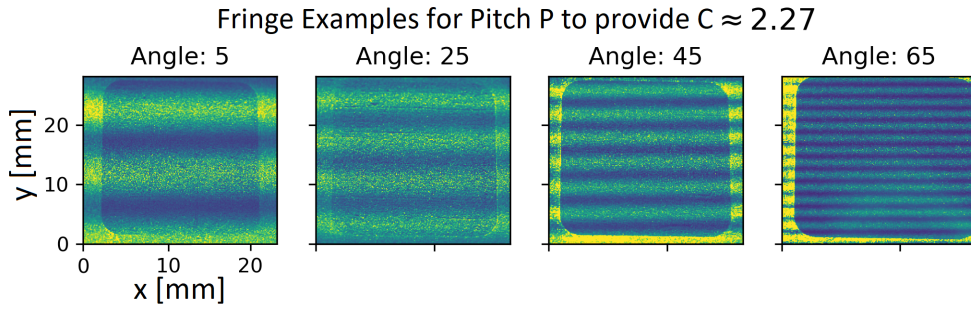The experimental procedure for DH measurements is described in detail below:

Figure 3: Fringe captures for $\theta = 5, 25, 45, 65°$, with appropriate fringe pitch P to achieve a phase-to-height calibration constant $C = 0.44[\text{mm/rad}]$.

1. The projector was angled and positioned according to the selected illumination angle.

2. A "pristine" powder bed was raked and positioned into the field of view of the camera.

3. A gamma calibration routine, described in [29, 33] was used to obtain an interpolation factor to ensure sinusoidal projected fringes and proper fringe contrast (avoiding over or under saturation).

4. Four sets of 15-bin fringes, with different fringe pitch P (pixels) were generated according to Equation 1, with every pixel intensity value altered by the gamma interpolator to maintain sinusoidality.

5. A phase-to-height calibration procedure was conducted to obtain the calibration constant C, for each fringe pitch P.

   - Phase maps of each fringe pitch were recorded for Keyence microscope stage heights of $\{-50.8, -25.4, 0, 25.4, 5.08\}\mu m$.

   - Gaussian filtered phase maps and the corresponding stage heights were used to develop linear calibration constants for each fringe pitch. An example calibration relationship is shown in Figure 4.

   - Fringe pattern pitch (in whole pixel values) was iteratively adjusted to normalize the phase-to-height calibration constants across all angles within 6% of the target, $\{0.22, 0.44, 0.94, 1.9\}$.

6. Phase maps were created using the steps outlined in Section 2.1 for each of the four fringe pitches P of two "pristine" powder surfaces, each raked parallel and perpendicular to the fringe projection direction, to be used as reference phase maps. A total of 15 iterations of images for each fringe were captured, later used to study the noise contributions from pixel intensity noise, and its impact on DH measurement.

7. Two more phase maps were created for each of the four fringe pitches P, on artificial PBDs created by raking the powder bed with the "defective" recoater blade in parallel and perpendicular directions with respect to the fringe projection direction, with 15 iterations of fringe images.

8. For each fringe pitch, four differential phase maps were created in total by subtracting each "pristine" reference phase map from each PBD phase map. This is repeated for each iteration.

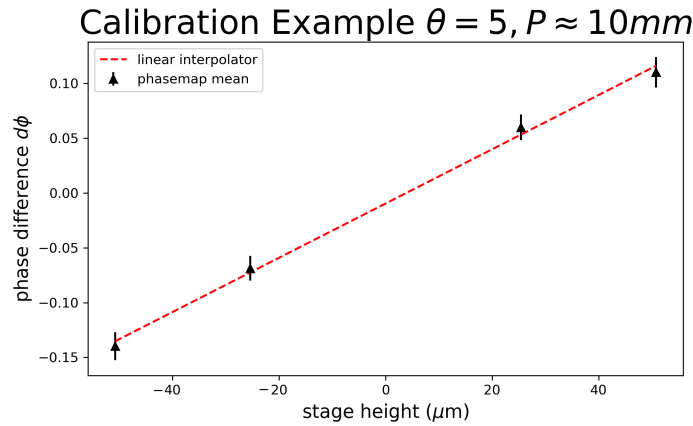9. Each differential phase map was converted to a DH map using the linear calibration constant C.

Calibration Example $\theta = 5, P \approx 10mm$

Figure 4: An example to showcase the phase-to-height calibration process. The black points represent the mean of the differential phase map across stage positions, with error bars representing a single standard deviation. The red dashed line shows the linear interpolator used to establish the phase-to-height calibration constant C.

10. Steps 1-8 were repeated for additional illumination angles.

To maintain consistent fringe contrast and sinusoidalality of fringe images, as well as produce accurate reference phase maps for every illumination angle, a "pristine" raked powder bed was used as the reference phase map. Due to the requirement of the reference phase map, PBD defects were re-made for each illumination angle.

To verify DFP measurement with absolute dimensions, two precision machines gauge blocks were purchased for measurement, a popular technique of structured light setup validation [34–36]. An 0.5mm thickness Mitutoyo calibration block (MTI-613506-531) was used to verify the DFP measurement setup, placed on an 8mm thickness block (MTI-613204-531) to serve as a reference, shown in Figure 5. Both calibration blocks were certified to grade 0, ordered from the catalog [37].

A spatial calibration technique was used to mitigate the camera skew, inevitable from the presence of the viewing angle. This allows the conversion from pixel coordinates to global coordinates, in order to compare measurement of the calibration block to the given specifications provided by Mitutoyo. Using homography, pixel locations of corners of the calibration block were selected, and a homography matrix was automatically generated to correct for viewing angle, a commonly used technique within the machine vision community [34–36]. This technique is applicable to the intended spatial calibration technique for *in-situ* sensor implementation, where the corners of the build platform can be used to establish a ground truth spatial pixel-to-global coordinate transformation matrix. Figure 6 shows the process and analysis of the calibration block measurement. Figure 6A shows the height map after pixel to millimeter transformation, hence the spatial units are in millimeters. The red and a yellow areas are sampled to estimate the noise field on the height measurement. A cross section in a dashed blue line, is represented in Figure 6B.

We observed excellent match between the calibration object height profile and the DFP monitoring system, shown in Figure 6A. The height standard deviation in within the red and yellow areas were $3.7\mu m$ and $4.0\mu m$, respectively. However, there is an inevitable artifact along the bottom edge of the calibration object, caused by the the camera viewing the "side" of the calibration block. During *in-situ* application, this effect will be reduced, as the powder bed surface is expected to be more continuous below $300\mu m$.
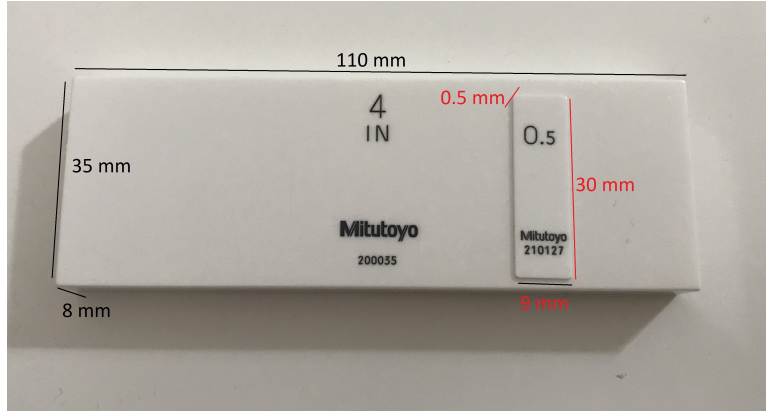
Figure 5: Mitutoyo Calibration block, gauge length 0.5 mm on top of the reference surface, an 8 mm thickness Mitutoyo block.
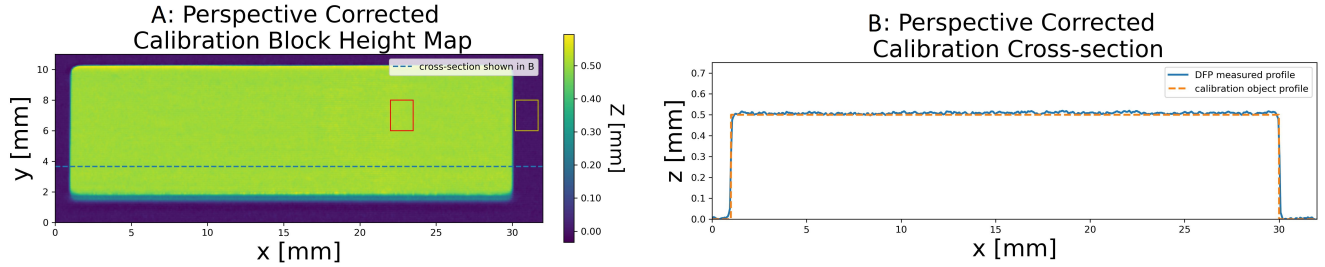

Figure 6: Measurement process of the Mitutoyo gauge block. A shows the corrected perspective calibration block height map, with millimeter spatial units obtained through the pixel-to-global transformation. Red and yellow areas were sampled to measure the noise field. The blue dotted line shows the cross-section represented in B, which is compared to the true height profile.

2.3   High-Pass Filtered Phase Measurements

In addition to DH measurements, data in the form of high-pass filtered phase measurements, referred herein as HPF measurements, are also presented. HPF measurements are made without reference phase maps and do not require the phase-to-height calibration step. HPF measurements instead rely on filtering out the low frequency carrier phase using a subtractive Gaussian filter to resolve localized PBD signatures. While these measurements were correleated to the full field topography of the surface, the HPF measurements can not be accurately converted to absolute height values; each pixel value is biased by neighboring pixels within the filter window. The benefit of reporting HPF measurements is that a quantative comparison of the effects of varying illumination angle θ on measuring the same PBD realization could be made, as opposed to to having to recreate the PBDs for every θ (a step needed in the DH measurements to obtain a "pristine" powder reference). The Keyence Microscope was used to verify the PBD defect heights to provide insight to the true defect heights resolved by the HPF method.

HPF measurement data was captured at the same illumination angles θ as the DH measurements, but did not include the phase-to-height calibration routine. To provide a fair comparison, incident fringe pitch P for all illumination angles was kept approximately consistent, as HPF relies on spatial averaging.

The experimental process of collecting HPF measurements was:

1. The projector was angled and positioned according to the selected illumination angle θ.

2. Gamma calibration and fringe pattern routines from steps 3 and 4 from Section 2.2 were followed

to produce fringe patterns with uniform contrast and corrected gamma for each illumination angle θ and fringe pitch P.

3. Fringe pitch P was iteratively selected to provide approximately uniform fringe pitch P (to the nearest whole pixel) on the measurement surface for each illumination angle.

4. The desired powder bed condition was created with one of the recoater blades: two "pristine" powder conditions (raked parallel and perpendicular to fringe direction), and two "defective" PBDs (also raked in both directions).

5. Sets of four spatial fringe pitches were generated according to Equation 1, with P adjusted for each angle to remain constant, and approximately $\{6.1, 12.2, 24.4, 48.8\}$ mm. This was different from the fringes produced in Section 2.2, where phase-to-height calibration was held constant across illumination angles θ.

6. A phase map was created according to Equation 5, and steps were repeated for each illumination angle θ.

   - To create the HPF measurement, the low frequency phase was filtered out of the phase map by subtracting a Gaussian filtered version of the phase map (using a spatial filter function from the openCV library [38] of size 91x91 pixels and standard deviation of 10 pixels or approximately 16 mm^2 with a standard deviation of 2.3 mm^2) from the original phase map.

7. After phase maps were recorded for each illumination angle θ, the Keyence microscope was used to estimate the PBD height values for comparison.

2.4   Single-Point Uncertainty Model

Previous work [39, 40] showcased the development and validity of a DFP measurement model used to simulate the measurement process and estimate DH uncertainty based on phase noise, and the contributions of pixel intensity noise during image capture. Intensity noise remains a dominant source of measurement uncertainty, and has been shown to dwarf other contributions such as spatial and intensity quantification [41], shown in our previous publication [40]. The model representing the linearized DFP operation was chosen for use; the requirements for which summarized in Section 2.1. In practice, this model produces the probability density function (PDF) of the uncertainty, and can be used to establish confidence intervals of every measurement point, statistically contributing to defect detection within the PBF process. Figure 10 shows the results of estimating DH uncertainty using the pixel intensity fluctuation occurring during the 15 iterations of DFP. The model relies on sampling the noise field on the camera pixels during the measurement process, and was used to establish confidence intervals for each height measurement point. The single-point uncertainty model used the DFP instrument transfer function to mathematically convert phase noise to height noise for each measurement pixel. The model was also able to represent the contributions on height uncertainty from the conversion of pixel intensity noise to phase noise.

Equation 9 is the PDF used to model the single-point DH measurement uncertainty χ_l with pixel intensity noise contributions [39, 40].

$$p(\chi_l) = \frac{e^{-z_3}\sec^2\frac{2\pi L\chi_l}{Pd}\left(1 + \sqrt{\pi}z_2 e^{z_2^2}\left(\mathrm{erf}\left(z_2\right)\pm 1\right)\right)L}{z_1\sqrt{1-\rho_{XY}^2}Pd}, \tag{9}$$

where

$$
\begin{aligned}
z_1 &= \frac{\sigma_Y^2 - 2\rho_{XY}\sigma_X\sigma_Y\tan\frac{2\pi L\chi_l}{Pd} + \sigma_X^2\tan^2\frac{2\pi L\chi_l}{Pd}}{\sigma_X\sigma_Y\left(1-\rho_{XY}^2\right)}, \\
z_2 &= \frac{\mu_Y\sigma_X\left(\rho_{XY}\sigma_Y - \sigma_X\tan\frac{2\pi L\chi_l}{Pd}\right) + \mu_X\sigma_Y\left(\sigma_X\rho_{XY}\tan\frac{2\pi L\chi_l}{Pd} - \sigma_Y\right)}{\sqrt{2}\sigma_X\sigma_Y\sqrt{1-\rho_{XY}^2}\sqrt{\sigma_Y^2 - 2\rho_{XY}\sigma_X\sigma_Y\tan\frac{2\pi L\chi_l}{Pd} + \sigma_X^2\tan^2\frac{2\pi L\chi_l}{Pd}}}, \\
z_3 &= \frac{\mu_Y^2\sigma_X^2 + \mu_X^2\sigma_Y^2 - 2\mu_X\mu_Y\sigma_X\sigma_Y\rho_{XY}}{2\sigma_X^2\sigma_Y^2\left(1-\rho_{XY}^2\right)},
\end{aligned}
\tag{10}
$$

and where $\mathrm{erf}(*)$ is the standard error function. Quantities L and d are geometrical values related to experimental setup (as seen in Figure 2A). P is the incident fringe pitch on the reference plane. Because the system was operating in the linear DFP regime, quantities L, d and P were combined and solved for during phase-to-height calibration constant C. Quantities σ_Y, σ_X, and ρ_{XY} are functions of measured pixel intensity noise shown in [39]. These quantities are intrinsically related to the standard deviation and correlation of random variables functionally related to ensembles of measured image intensities across iterations from an experiment. Correlation in the noise structure may arise from periodic lighting fluctuations such as overhead fluorescent lights, projector gamma error, or dust particle patterns on either optics lenses. Also shown in detail in our previous work, the evaluation of $p(\kappa)$ required separation into two integration regions, where the minus sign $(-)$ when $|\chi| < \frac{\pi P(d-z)^2}{2\left(2\pi Ld + \frac{1}{2}\pi P(d-z)\right)}$, and taking the plus sign $(+)$ when $\frac{\pi P(d-z)^2}{\left(2\pi Ld + \frac{1}{2}\pi P(d-z)\right)} > |\chi| > \frac{\pi P(d-z)^2}{2\left(2\pi Ld + \frac{1}{2}\pi P(d-z)\right)}$.

2.5 Measurement Parameter Selection

For *in-situ* PBF monitoring, it is important to select measurement parameters such as illumination angle θ, bin number n, and fringe pitch P to establish measurement sensitivity allowing for detection of PBDs during the process [26]. In order to estimate the uncertainty field on DFP measurements, the PDF Equation 9 from Section 2.4 was used to establish fundamental central tendency and dispersion characteristics of the height error,

$$
\begin{aligned}
E(\chi_l) &= \int_{-\infty}^{\infty}\chi_l p(\chi_l)dx \tag{11} \\
Std(\chi_l) &= \sqrt{\int_{-\infty}^{\infty}[\chi_l - E(\chi_l)]^2 p(\chi_l)dx}, \tag{12}
\end{aligned}
$$

where χ_l is the DH measurement noise/error variable. With these expressions, the ideal DH single point standard deviation was calculated for the average level of pixel intensity noise, and used to determine the fringe P selected for each experimental setup. For reference, the experimental fringe contrast was approximately 90 units of pixel intensity; with an average standard deviation of 1.67 pixel intensity
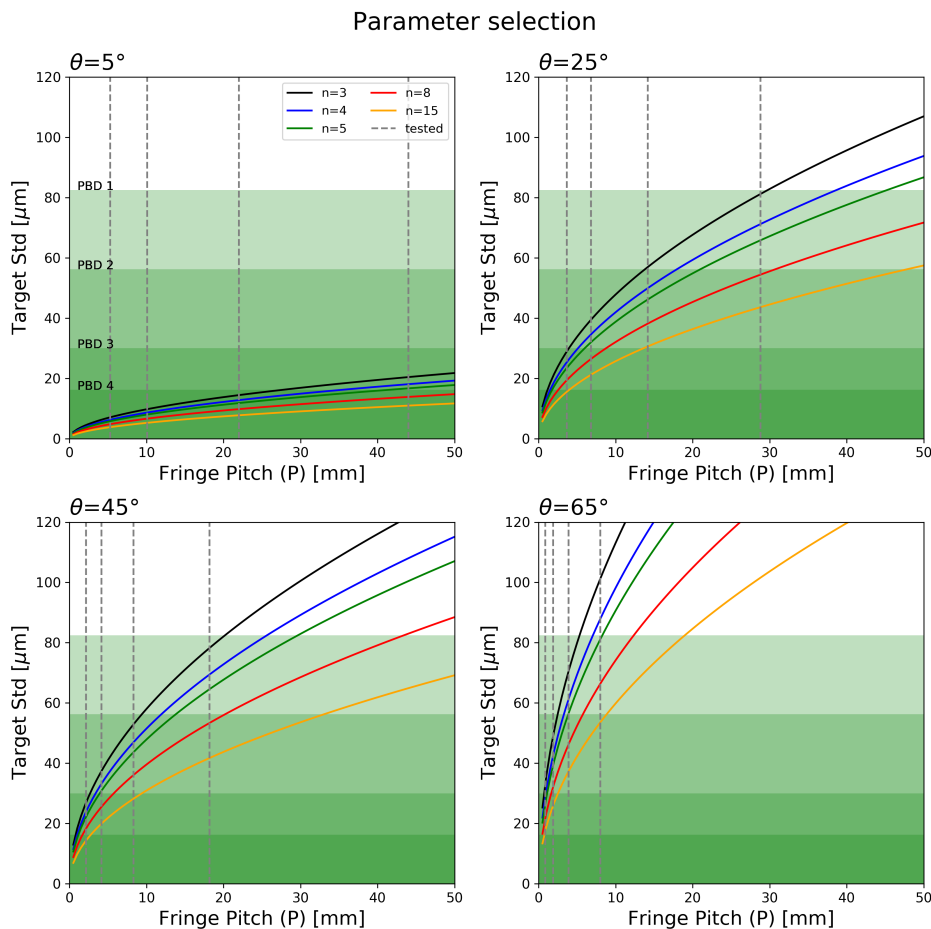
Figure 7: Parameter selections of the experiment with varying bin number N, fringe pitch P, and illumination angle θ. The green shaded areas show the regions of minimum required noise to resolve PBDs with heights characteristic of experiment.

units, that equates to an average of .0186 pixel noise (normalized by fringe contrast). Significantly higher fringe contrast was achieved for illumination angles $\theta > 25°$, but for the sake of consistency, a contrast value achievable by all measurement angles was selected.

Figure 7 shows the selected parameters for experiment for all four illumination angles θ, all four fringe pitches P, and all five fringe projection bin numbers N. The green shaded areas correspond to DFP resultant height noise approximately 1/2 of the measured height of each PBD streak, which the authors argue is the minimum sensitivity required to detect a single pixel sized PBD with 95% confidence. The colored series lines show how the ideal standard deviation of measurement increases for increasing fringe pitch P, for a range of bin numbers N. The gray dashed lines shows the selected P for each angle; each four representing similar resultant calibration constants.

3   Results and Discussion

To showcase the effects on noise field measurements from multiple DFP parameters, quantitative measures of experimental measurement noise compared to simulation are presented, as well as qualitative data to illustrate the full-field noise structures which arise from certain non-ideal parameters. Qualitative analysis on the noise structures observed on HPF datasets are also presented.
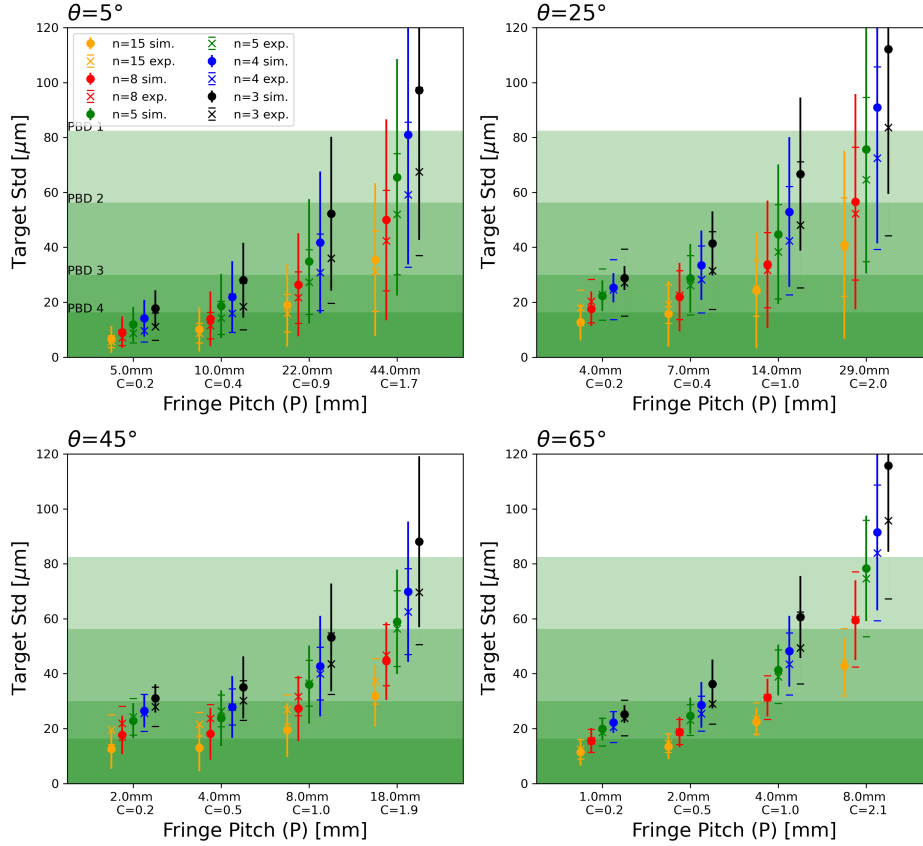
Measurement Noise: Model & Experiment

Figure 8: Measured DH noise across iterations for a range of illumination angles θ, bin number N, fringe pitch P. Green areas show the minimum experimental value of uncertainty required to detect a single pixel of the corresponding PBD at 95% (or 2σ) confidence. Experimental points are shown with error bars of a single standard deviation. Uncertainty model estimations are shown with filled circle markers.

3.1 Differential Height Uncertainty

To summarize our findings across every combination of tested parameters, the noise distributions of ensemble experimental DH measurements was compared to the estimated single-point uncertainty. Figure 8 shows the estimated and experimental average noise fields on DH measurements across θ, N, P. Estimated DH measurement noise is shown with filled circles and solid bars representing a single standard deviation, and the experimental full field noise median is shown with X's and errorbar caps representing a single standard deviation. The green areas in the figure correspond to minimum levels of DH noise required to detect the corresponding PBD, at a 95% confidence interval for a single measurement point.

The uncertainty model summarized the average observed noise levels of the experiments, with agreement for each parameter combination within a single standard deviation. For measurement parameters across all θ, for $N > 5$ and calibration constant $C < 1.7$, the measurement model estimated the experiment very accurately. When P increases (for equivalently $C > 1$), the model begins to erroneously overestimate the measurement noise, which becomes large enough to impact the most severe PBD streaks. A higher discrepancy between the model estimations and the experimental noise for $n < 5$ was also observed, expectedly so as a results of inadequate sinusoidality of projected fringes

during low bin number measurement.

Figure 8 shows noise levels positively correlated with P, due to decreased phase-to-height sensitivity. This phenomenon is present across all θ, though the noise fidelity was most impacted by P for the $\theta = 65$ case, potentially due to specular reflections of the powder bed contributing to poor fringe intensity response. Increasing P shows a substantial increase in the variability of the noise, shown by increasing amplitudes of error bars, an effect further illustrated in Section 2.2.

Bin number N also directly affected the DH measurement uncertainty, inversely correlated to the DH noise field. The negative effects of lowering n are exacerbated in cases of the largest P for each θ. Together, inadequate DFP parameters such as P and N can drastically increase DH uncertainty to levels past appropriate signal-to-noise ratios for *in-situ* PBF defect monitoring, also creating large discrepancies in the model uncertainty predictions.

The full field noise structures of DFP and how they are affected by parameters N and P are presented for a representative example of the DH measurement with $\theta = 45°$ in Figure 9. Figure 9A shows the DH measurements for parallel-to-fringe direction PBDs, and Figure 9B shows the standard deviation of each DH measurement, across the 15 iterations of DFP measurements recorded. The percentage values within Figure 9B show the average reduction in DH standard deviation when compared to the previous image (normalized per added bin N).

DH measurements shown in Figure 9A resolve the PBD realizations with different noise fields as functions of P and N. In agreement with Figure 8, the full field detection of PBDs was improved by increasing N and decreasing P. Data produced with high bin number ($N > 5$) across all P contained low background noise fields, in which the PBDs 1-3 were resolved. Even with high bin number and low P, PBD 4 (characteristic height of $20 - 45\mu m$) was difficult to resolve, appearing faintly, with background noise reducing resolution for $P > 4$mm. Data produced with mid-range bin number ($N = 4, 5$) showed more sensitivity to P, and in cases where $P > 4.2$mm, PBD 3 became lost in background noise. PBD resolution became especially poor for combinations of low bin number ($N = 3$) and mid-to-high pitch ($P > 8.5$mm), where PBD 2 was poorly resolved due to background noise.

In Figure 9B, the DH measurement noise for each parameter combination, across all 15 iterations, is given. In agreement with Figure 8, noise fields increased with P and inversely with N. However, the measurement fidelity gains of adding bins reduced as N increased. Figure 9B shows the decrease in average DH measurement noise per added bin was similar across all P. Structured noise levels were be observed for low bin number ($N < 5$), and was especially severe for $P > 8.5$mm. This phenomenon explains the large errorbars seen for low N and high P in Figure 8, and motivates redundancy (adding more bins) to mitigate the specular behavior of the stainless steel powder bed. These noise structures can contribute to erroneous false positives of PBD measurement during *in-situ* DFP monitoring. Heightened levels of DH measurement noise in areas of the PBDs were also observed, suggesting that the geometry, or nonuniform surface structure, influences the DFP process. This phenomenon was further imaged and explored in Figure 10 and Section 2.3.

To showcase an example of the model's estimation of DH uncertainty, a representative case comparing observed DH noise across all 15 iterations and estimated uncertainty is presented in Figure 10. Figure 10A shows the measured standard deviation of DH measurements across all iterations, for an example measurement with $N = 5$, $\theta = 45°$, and $P \approx 17$mm. Figure 10B shows the estimated standard deviation of the PDF produced by the single point uncertainty model (Equation 9) for the
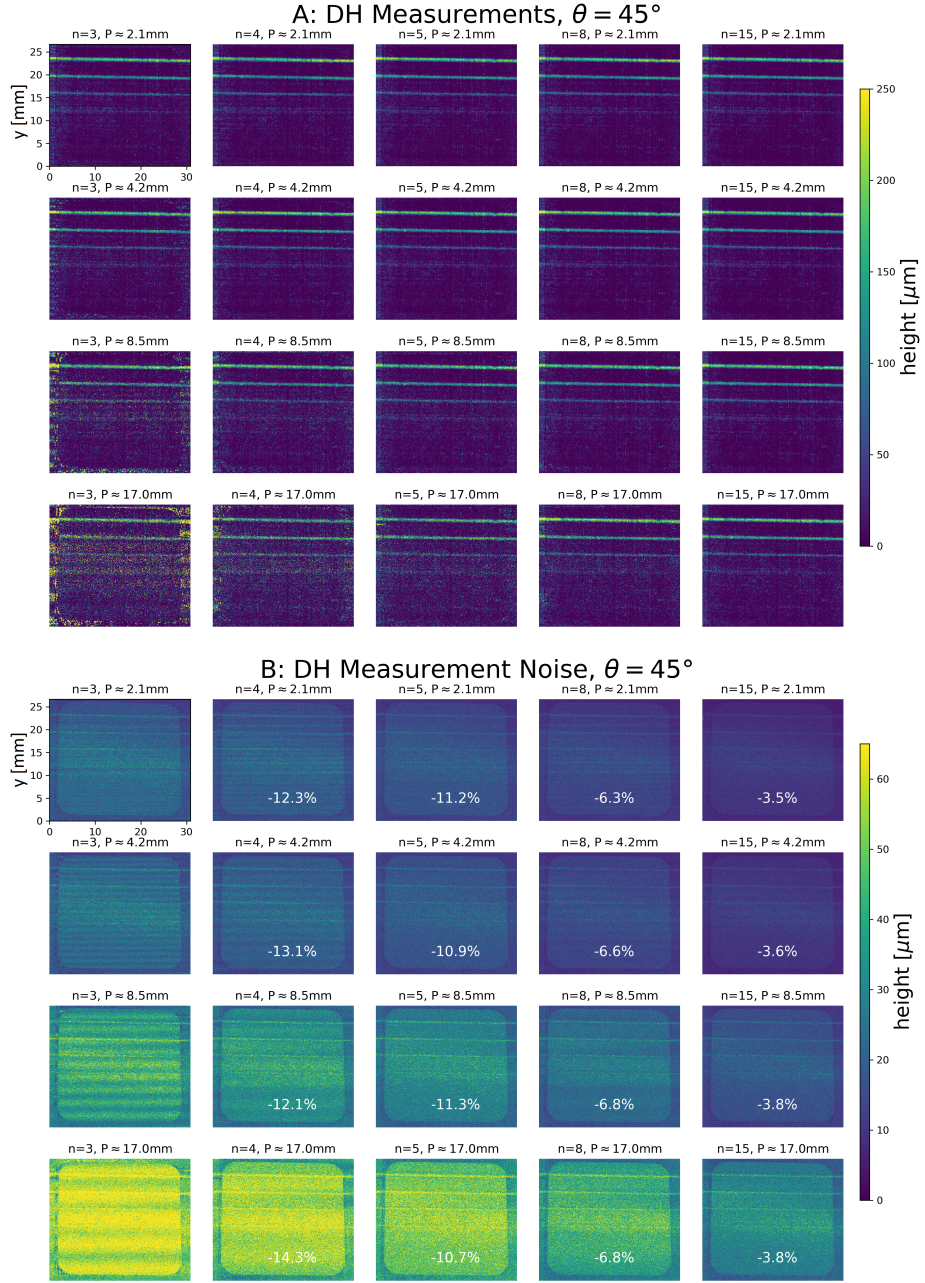
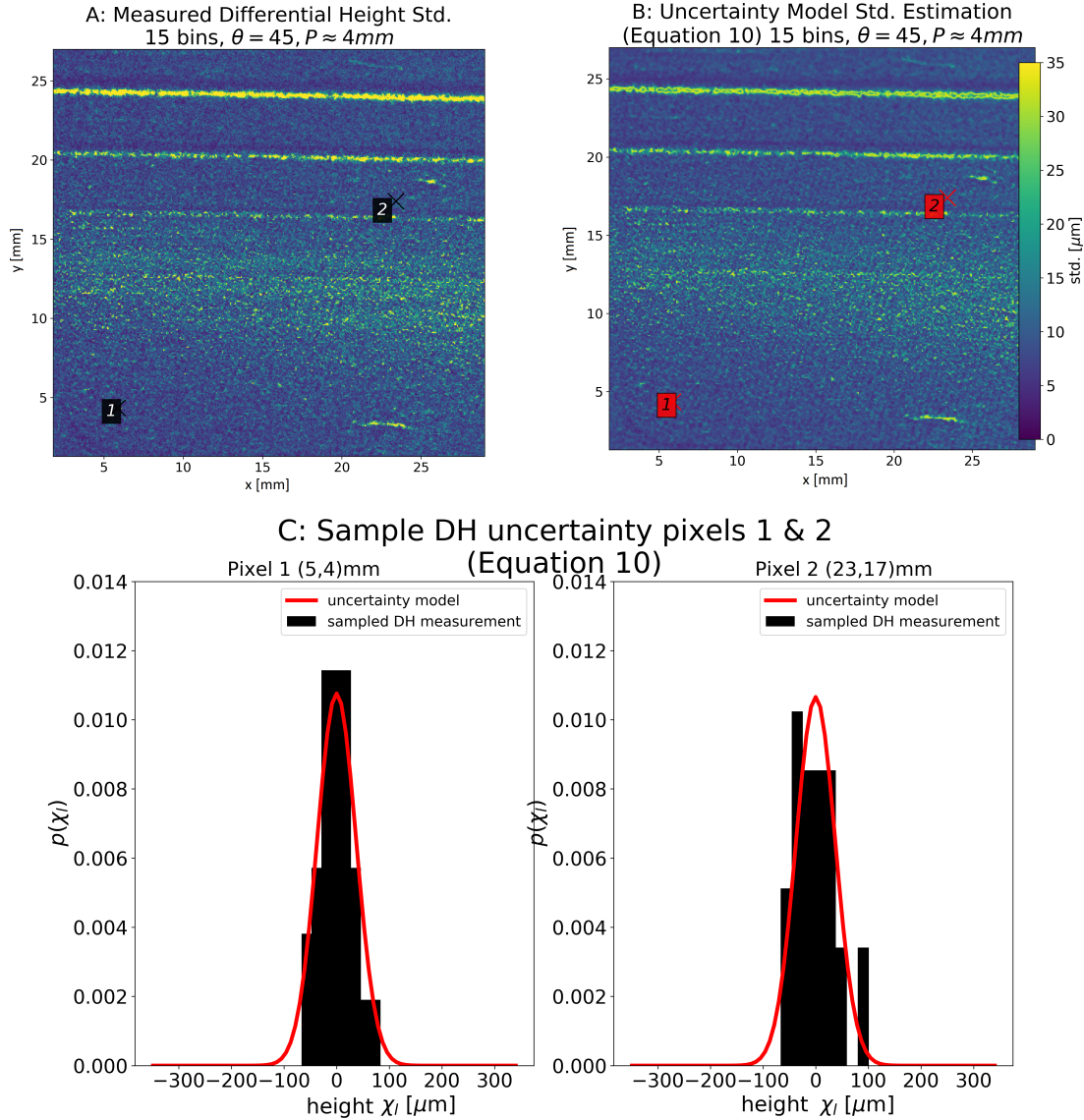**Figure 9:** Effects on DH measurements of reducing bin number

Figure 10: Full field differential height measurement noise of an example "pristine" powder condition. A: measured differential height noise across iterations. B: estimated differential height uncertainty made by the single point uncertainty model. C: estimated PDFs for local sample pixels 1 and 2 in A and B.

same measurement parameters. Figure 10C shows the distribution of the DH measurements and the estimated uncertainty distribution of sample points 1 and 2 from Figure 10A-B.

Observed in Figure 10A, DH measurement noise was non-uniform across the field of measurement, and varied dramatically depending on subtle surface textures. The uncertainty model captured these noise structures, seen in Figure 10B, allowing for pixel-by-pixel statistical confidence to determine the probability of each height point. The distributions of DH noise and estimated uncertainty of example pixels 1 and 2 is shown in Figure 10C, showcasing excellent agreement between model and simulation.

3.2   High-Pass Filtered Measurement

Illumination angle is another key parameter in which we explored. This factor plays an important role in the phase-to-height relationship, determining the $d : L$ ratio in Equation 7. In general, a smaller
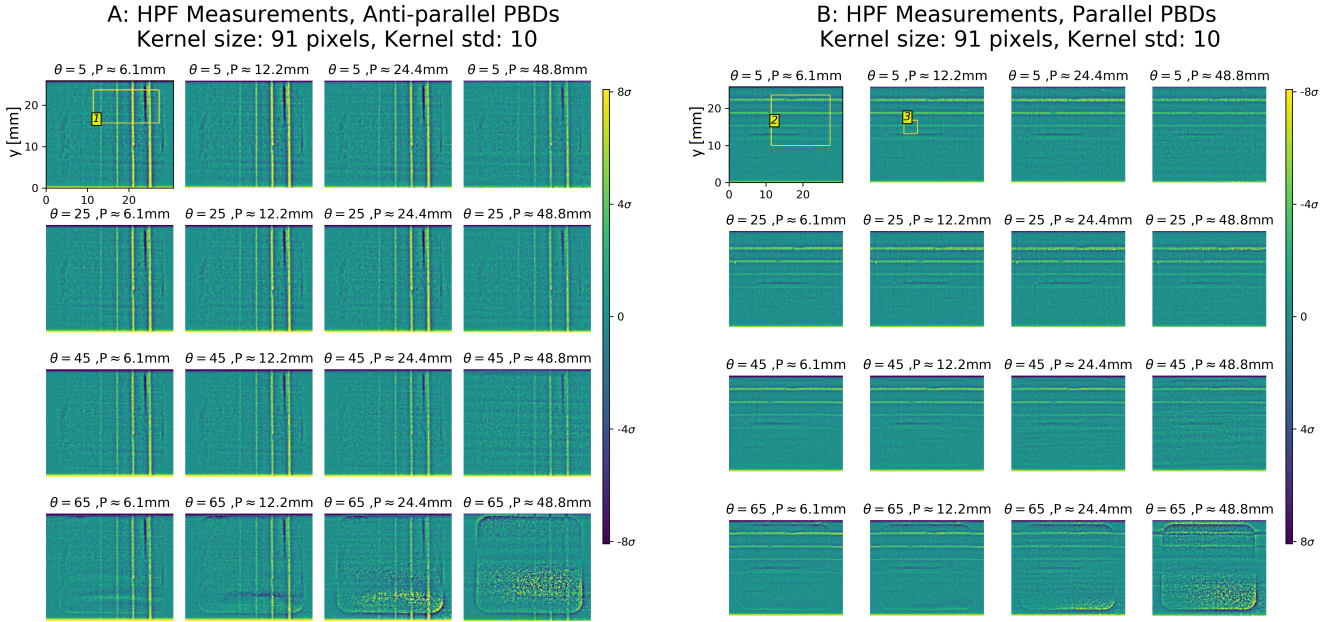
Figure 11: HPF measurements across illumination angles and fringe pitch. A shows perpendicular PBDs to fringes, B shows parallel PBDs to fringes. Colorbar limits are based on ±8 standard deviations of noise fields across all 15 iterations. Areas 1-3 are represented in blown up view in Figures 12 and 13

.

illumination angle θ (measured from the horizon) will provide phase maps with greater height sensitivity, allowing for a larger spatial fringe pitch P to achieve the same phase-to-height calibration constant C, as discussed in Section 2.2. Fringes with larger P can be especially useful when spatial pixel intensity averaging is needed to reduce noise, but must not influence the sinusoidallity of projection patterns by filter size approaching the spatial period of illumination. Requirements for small P to achieve adequate phase-to-height sensitivity combined with out-of-focus projection can also adversely influence fringe contrast, or even potentially blur fringe projection altogether. During experiments, the illumination angle also affected other crucial experimental factors such as fringe contrast, while also potentially adding areas of measurement shadowed by out-of plane features.

In order to fairly isolate θ, and observe its impacts on DFP measurement, HPF measurements with varying θ for a single PBD realization are presented. By filtering out the carrier phase using a Gaussian filter (the process summarized in Section 2.3), the need for a reference phase map is eliminated, thus allowing the same PBD realization to be used for each θ. Figure 11A-B shows HPF results across a range of θ and P for PBDs created perpendicular and parallel to fringe projection direction, respectively. Figure 12A-B shows zoomed-in regions of the HPF results presented in Figure 11A-B. Figure 13A-B shows local region noise structures that were observed for certain θ and P. Each HPF result presented is shown with colorbar limits of ±8 standard deviations, for fair visual comparison. Due to the lack of absolute height values of the HPF measurements, the Keyence microscope was used to verify the height of defects by providing profiles across the detected streak PBDs, reporting heights of approximately $150-180\mu m, 105-120\mu m, 45-75\mu m, 20-45\mu m$ for PBD 1–4, respectively.

Figure 11 shows clear differences in measurement fidelity as functions of θ and P. Because we kept P constant across all θ, the DFP measurement parameters from θ=5,$P \approx 6.1$mm contributed to the most height-sensitive phase map. The outcome of this sensitivity was a clear out-of-plane
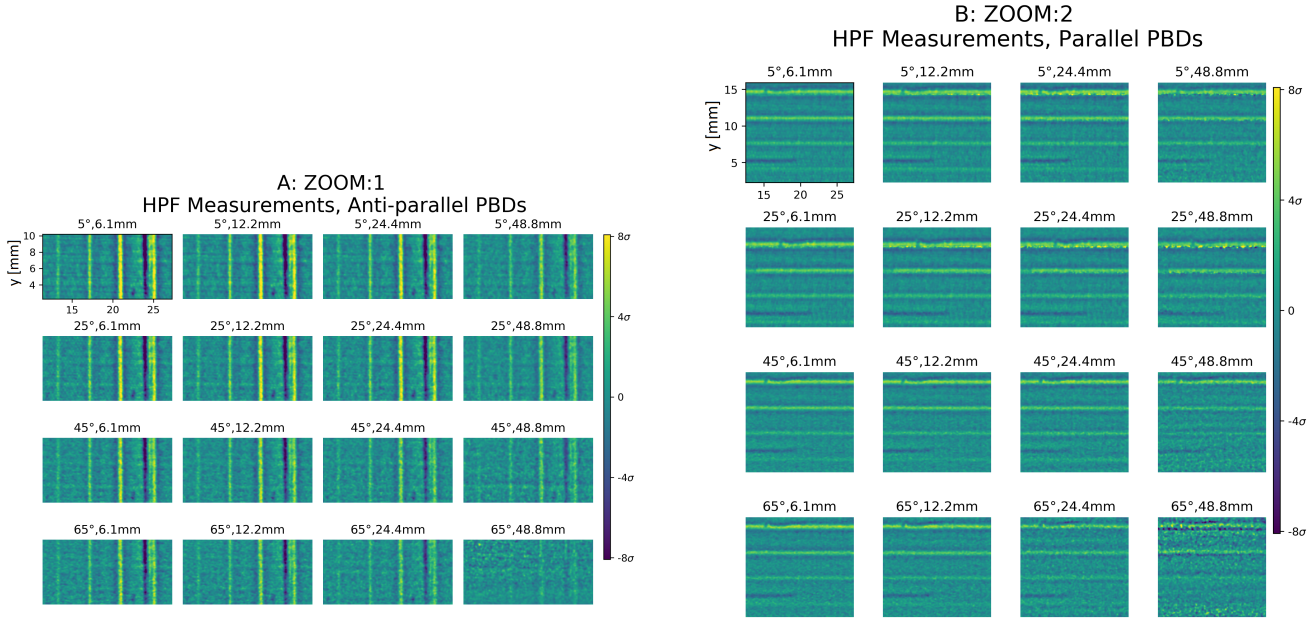
Figure 12: HPF measurements across illumination angles and fringe pitch for areas 1 and 2 in Figure 11. A shows perpendicular PBDs to fringes, B shows parallel PBDs to fringes.

imaging of all four PBD streaks, with very high signal-to-noise ratio (SNR). This effect can be seen in both PBD directions presented, independent of PBD direction. As θ was increased, the phase-to-height sensitivity decreased, apparent in the less resolved PBDs, consistent for all periods and both PBD directions. Increasing P also resulted in decreased PBD resolution, eventually producing noise fields strong enough to block detection of the smaller PBDs for $\theta = 5, 25, 45°$, though the largest PBDs were able to be resolved. Severe HPF noise artifacts were observed in both PBD directions for $\theta = 65°$, $P = 24.4, 48.8mm$. Illumination at $\theta = 65°$ coupled with very large P (around twice the size of powder measurement area) is shown to be problematic for HPF results.

Within each row of constant θ, larger P equated to lower phase-to-height sensitivity, with the potential to dwarf the PBDs in noise. For cases $\theta = 45, 65°$ and values $P \approx 24.4, 48.8$, the fringe-to-height sensitivity was so poor that noise within localized regions significantly impact the resolution of all four PBDs, and in the worst cases completely obscured the smallest PBD (approximate height of $20 - 45\mu m$). This presents considerable issues for in-situ deployments in PBF machines with physical constraints that limit the possible range of of projection angle.

Powder recesses were also easily resolved by the HPF method, as shown in Figure 12A-B, where such a PBD existed in different locations, represented by a negative phase value. This recess PBD was not intentional; but it was chosen to keep the defect in the PBD realization, as this type of powder recess could contribute to final build defects such as keyhole porosity [22] initiated by large VED. An artifact of the HPF method was the exaggeration of PBD phase values resulting in non-uniform powder layers which occurred with the spatial averaging window. This phenomenon was exaggerated because the spatial kernel was influenced by both positive and negative phase vales, increasing both PBD area's absolute phase values.

Far outlier measurement points appeared in HPF results of the parallel PBDs for certain illumination angles. Seen in Figure 12B, HPF results $\theta = 5, 25°$ show these far outlier phase pixels, just below the two largest PBDs. These artifacts are likely caused by inadequate fringe illumination caused by the
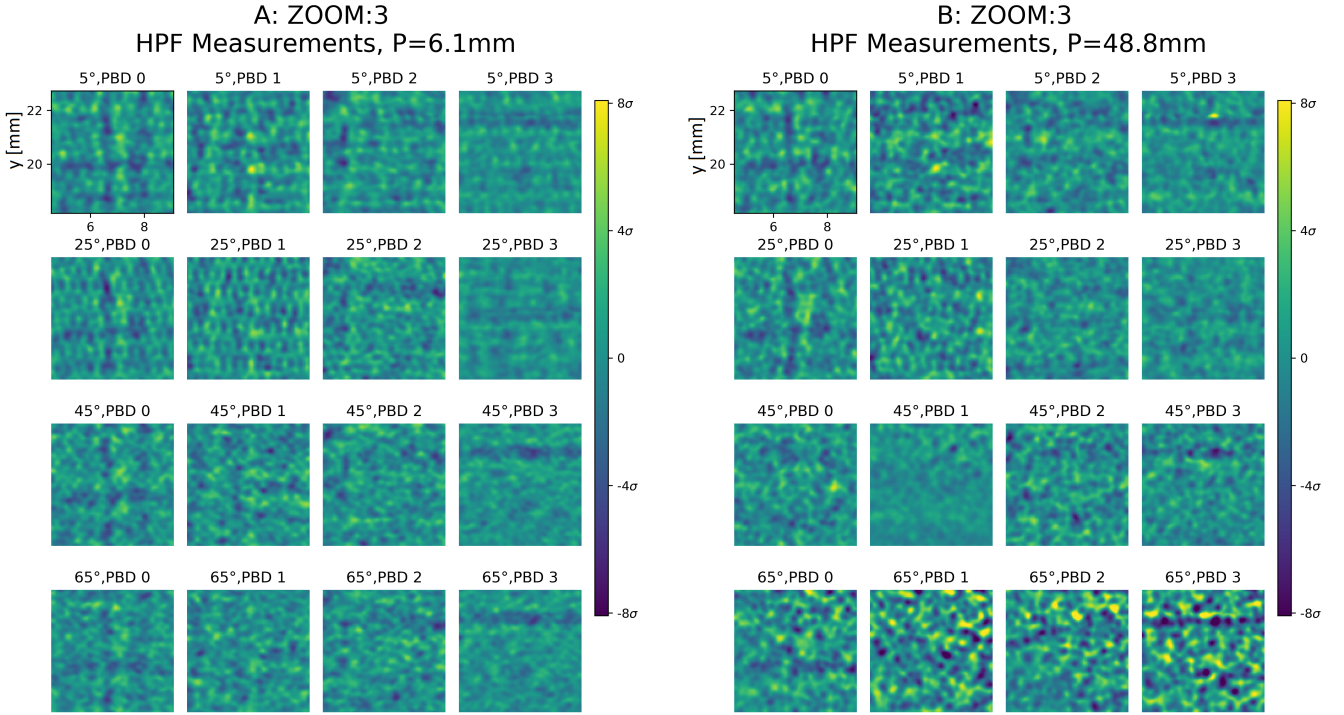
Figure 13: HPF measurements across all illumination angles and for different PBD realizations. A shows small pitch P and the occurrence of "diamond" shaped noise structures. B shows the same PBDs and illumination

PBD geometry either blocking projection, or at least interfering with projection sinusoidality. Data taken with $\theta = 45, 65°$ did not have this issue, as the height of PBDs did not geometrically impact DFP measurement.

Another experimental difference was noticed for varying θ: fringe contrast. This parameter is significant within the DFP process, as the contribution of pixel noise is divided by fringe contrast within phase map creation [39, 40]. For illumination angles $\theta = 5, 25°$, the camera required a significantly increased aperture f-number (approximately set to $f/2$) to achieve a fringe contrast of 90, while the aperture was closed to above $f/5$ for illumination angles $\theta = 45, 65°$. An explanation for this effect is the significant reflective properties of the metallic powder measurement surface. However, to eliminate the fringe contrast variable, and the resultant noise contributions from pixel intensity noise, were kept constant (contrast values were reported within 3% for the HPF measurements).

In addition to decreased fringe contrast, HPF measurements at illumination angle $\theta = 5, 25°$ included artifacts. Figure 13A-B shows a zoomed-in view of area 3 in Figure 11B, to illustrate the localized surface behavior of HPF measurement. Figure 13A-B provided results across different PBD realizations and θ, for $P \approx 6.1$mm (A) and $P \approx 48.8$mm (B).

Figure 13A shows the local noise structure of HPF measurements of the powder bed for several realizations, for the smallest fringe pitch tested, $P \approx 6.1$mm. For low illumination angles $\theta = 5, 25°$ and small P, a diamond-shaped noise structure can be observed, absent in larger P (Figure 13B). This structure was independent of Gaussian kernel size, or standard deviation. As seen in $P \approx 6.1$mm, $\theta = 5, 25°$, the diamond pattern was observed to be periodic, with a period of approximately 200μm. The origin of these artifacts are unknown at the time of this study, but have appeared in each measurement at $\theta = 5, 25°$ for $P < 25$mm, mitigated by larger spatial fringe pitch P

4   Conclusions

In this study, DFP measurements were performed on PBDs created in the lab using conditions designed to mimic the PBF recoating process. Measurements were made across several parameters, e.g. bin number N, fringe pitch P, and illumination angle θ. The uncertainty estimation of the single point uncertainty model was tested by comparing the estimated DH measurement uncertainty to ensemble DH measurements made with the prototype monitoring system. Full field DH measurement phenomena were observed and presented, including error structures, which arose from non-ideal measurement parameter combinations. High-pass filtered DFP phase maps were also reported to gain insight on the form of noise structures of HPF measurement.

Agreement between the noise field estimations produced by the single point uncertainty model and the experimental DH variation within a single standard deviation was witnessed, and closer agreement to realistic measurement parameters (adequate bin number n and fringe pitch P required to resolve our lab-created PBDs). The model presented can be used to establish optimal measurement parameters for DH measurement, as well as provide a statistical confidence of every measurement point to reduce false positive PBD detections.

To gain insight on the full field noise structures of DH measurements and the impacts on PBD resolution, a test case was presented with varying bin number n and fringe pitch P and $\theta = 45°$. The negative impacts on DH noise for inadequate combinations of measurement parameters was showcased, and PBD detection limits for the DFP monitoring system were determined for a range of four levels of PBD severity.

To isolate the effects of illumination angle θ, reference-free HPF full field DFP measurements were reported. While the results from $\theta = 5, 25$ and smallest fringe pitch contribute to phase maps which were the most sensitive to height profile, structured noise not present in larger pitch HPF measurement was observed. A possible explanation for this phenomenon is the reflective properties of the stainless steel powder creating specular artifacts at low illumination angles with low fringe pitch.

The experimental results and modeling herein provides motivation for best practices of PBD detection using a DFP monitoring system. The results show illumination angle should be $\theta > 25°$ to avoid erroneous specular artifacts in the powder bed. These low illumination angles also proved difficult to obtain the same levels of fringe contrast as $\theta = 45°, 65°$, which amplified pixel intensity noise. No adverse effects on measurement fidelity for small fringe pitch P was observed, and due to the increased height sensitivity, this parameter should be minimized within the limits of projection contrast. Larger bin number N also contributes to improved measurement fidelity, though requires a longer image acquisition time. The results showed decreasing benefits of adding bins to measurements, as average noise reductions of less than 4% per bin past $N = 15$ were measured.

In summary, feasibility for *in-situ* powder bed monitoring using the DFP method has been shown. DFP systems, often an order of magnitude less expensive than other profiling techniques such as coherent light scanning, provide a rapid method of part health monitoring when either mounted within the powder bed chamber, or mounted just outside the chamber if two view ports are available. Further research includes the real-time operation of this monitoring technique during MAM.

Acknowledgement

References

[1] V. Sriram, V. Shukla, and S. Biswas, "Metal Powder Based Additive Manufacturing Technologies—Business Forecast," in 3D Printing and Additive Manufacturing Technologies, pp. 105–118, Springer, 2019.

[2] S. Mohd Yusuf, S. Cutler, and N. Gao, "The impact of metal additive manufacturing on the aerospace industry," Metals, vol. 9, no. 12, p. 1286, 2019.

[3] A. Gisario, M. Kazarian, F. Martina, and M. Mehrpouya, "Metal additive manufacturing in the commercial aviation industry: A review," Journal of Manufacturing Systems, vol. 53, pp. 124–149, 2019.

[4] W. E. Frazier, "Metal additive manufacturing: a review," Journal of Materials Engineering and performance, vol. 23, no. 6, pp. 1917–1928, 2014.

[5] J. C. Najmon, S. Raeisi, and A. Tovar, "Review of additive manufacturing technologies and applications in the aerospace industry," Additive manufacturing for the aerospace industry, pp. 7–31, 2019.

[6] B. M. Colosimo, S. Cavalli, and M. Grasso, "A cost model for the economic evaluation of in-situ monitoring tools in metal additive manufacturing," International Journal of Production Economics, vol. 223, p. 107532, 2020.

[7] "Additive Manufacturing: Building the Future," 2019.

[8] J. Fielding, A. Davis, B. Bouffard, M. Kinsella, T. Delgado, J. Wilczynski, K. Marchese, and I. Wing, "Department of defense additive manufacturing roadmap," US Department of Defense, Washington, DC, 2016.

[9] D. Thomas, "Economics of the us additive manufacturing industry," NIST Special Publication, vol. 1163, 2013.

[10] X. Lin, K. Zhu, J. Y. H. Fuh, and X. Duan, "Metal-based additive manufacturing condition monitoring methods: From measurement to control," ISA Transactions, 2021.

[11] M. Seifi, A. Salem, J. Beuth, O. Harrysson, and J. J. Lewandowski, "Overview of materials qualification needs for metal additive manufacturing," Jom, vol. 68, no. 3, pp. 747–764, 2016.

[12] M. Grasso and B. M. Colosimo, "Process defects and in situ monitoring methods in metal powder bed fusion: a review," Measurement Science and Technology, vol. 28, no. 4, p. 44005, 2017.

[13] Y. Liu, L. A. Blunt, F. Gao, X. Jiang, Z. Zhang, G. Saunby, J. Dawes, B. Blackham, H. A. Rahman, and C. Smith, "In-Situ Areal Inspection of Powder Bed for Electron Beam Fusion AM System Based on Fringe Projection," in Proceeding of ASPE/euspen Summer Topical Meeting: Advancing Precision in Additive Manufacturing, 2018.

[14] Y. Liu, L. Blunt, Z. Zhang, H. A. Rahman, F. Gao, and X. Jiang, "In-situ areal inspection of powder bed for electron beam fusion system based on fringe projection profilometry," Additive Manufacturing, vol. 31, p. 100940, 2020.

[15] Z. Li, X. Liu, S. Wen, P. He, K. Zhong, Q. Wei, Y. Shi, and S. Liu, "In situ 3D monitoring of geometric signatures in the powder-bed-fusion additive manufacturing process via vision sensing methods," Sensors (Switzerland), vol. 18, no. 4, p. 1180, 2018.

[16] M. Seita, "A high-resolution and large field-of-view scanner for in-line characterization of powder bed defects during additive manufacturing," Materials & Design, vol. 164, p. 107562, 2019.

[17] D. B. Pedersen, E. R. Eiríksson, H. Aanaes, and H. N. Hansen, "In-situ monitoring in additive manufacturing using contact image sensors," in Proceedings of the ASPE/EUSPEN 2016 Summer Topical Meeting on Dimensional Accuracy and Surface Finish in Additive Manufacturing. ASPE–The American Society for Precision Engineering, 2016.

[18] J. L. Bartlett, B. P. Croom, J. Burdick, D. Henkel, and X. Li, "Revealing mechanisms of residual stress development in additive manufacturing via digital image correlation," Additive Manufacturing, vol. 22, pp. 1–12, 2018.

[19] J. L. Bartlett, A. Jarama, J. Jones, and X. Li, "Prediction of microstructural defects in additive manufacturing from powder bed quality using digital image correlation," Materials Science and Engineering: A, p. 140002, 2020.

[20] M. Bayat, A. Thanki, S. Mohanty, A. Witvrouw, S. Yang, J. Thorborg, N. S. Tiedje, and J. H. Hattel, "Keyhole-induced porosities in Laser-based Powder Bed Fusion (L-PBF) of Ti6Al4V: High-fidelity modelling and experimental validation," Additive Manufacturing, vol. 30, p. 100835, 2019.

[21] P. J. DePond, G. Guss, S. Ly, N. P. Calta, D. Deane, S. Khairallah, and M. J. Matthews, "In situ measurements of layer roughness during laser powder bed fusion additive manufacturing using low coherence scanning interferometry," Materials & Design, vol. 154, pp. 347–359, 2018.

[22] L. Scime and J. Beuth, "Anomaly detection and classification in a laser powder bed additive manufacturing process using a trained computer vision algorithm," Additive Manufacturing, vol. 19, pp. 114–126, 2018.

[23] M. Aminzadeh and T. Kurfess, "Vision-based inspection system for dimensional accuracy in powder-bed additive manufacturing," in International Manufacturing Science and Engineering Conference, vol. 49903, p. V002T04A042, American Society of Mechanical Engineers, 2016.

[24] M. Heinl, F. K. Schmitt, and T. Hausotte, "In-situ contour detection for additive manufactured workpieces," Procedia CIRP, vol. 74, pp. 664–668, 2018.

[25] T. G. Fleming, S. G. L. Nestor, T. R. Allen, M. A. Boukhaled, N. J. Smith, and J. M. Fraser, "Tracking and controlling the morphology evolution of 3D powder-bed fusion in situ using inline coherent imaging," Additive Manufacturing, vol. 32, p. 100978, 2020.

[26] B. Zhang, J. Ziegert, F. Farahi, and A. Davies, "In situ surface topography of laser powder bed fusion using fringe projection," Additive Manufacturing, vol. 12, pp. 100–107, 2016.

[27] M. Kalms, R. Narita, C. Thomy, F. Vollertsen, and R. B. Bergmann, "New approach to evaluate 3D laser printed parts in powder bed fusion-based additive manufacturing in-line within closed space," Additive Manufacturing, vol. 26, pp. 161–165, 2019.

[28] M. Halioua and H.-C. Liu, "Optical three-dimensional sensing by phase measuring profilometry," Optics and Lasers in Engineering, vol. 11, no. 3, pp. 185–215, 1989.

[29] S. Zhang, High-Speed 3D Imaging with Digital Fringe Projection Techniques. CRC Press, USA, 2016.

[30] T. Hoang, B. Pan, D. Nguyen, and Z. Wang, "Generic gamma correction for accuracy enhancement in fringe-projection profilometry," Optics Letters, vol. 35, no. 12, pp. 1992–1994, 2010.

[31] H. Guo, H. He, and M. Chen, "Gamma correction for digital fringe projection profilometry," Applied Optics, vol. 43, no. 14, pp. 2906–2914, 2004.

[32] S. Ma, C. Quan, R. Zhu, L. Chen, B. Li, and C. J. Tay, "A fast and accurate gamma correction based on Fourier spectrum analysis for digital fringe projection profilometry," Optics Communications, vol. 285, no. 5, pp. 533–538, 2012.

[33] M. O'Dowd, Niall M; Todd, "Out-of-Plane Surface Measurement and Porosity Quantification Using Fringe Projection Structured Light System for use in Powder Bed Manufacturing," in Metal Additive Manufacturing Conference, pp. 229–238, 2019.

[34] P. Bamrungthai and P. Wongkamchang, "A novel method for camera calibration and image alignment of a thermal/visible image fusion system," in Fourth International Conference on Photonics Solutions (ICPS2019), vol. 11331, p. 113310H, International Society for Optics and Photonics, 2020.

[35] S. A. K. Tareen and Z. Saleem, "A comparative analysis of sift, surf, kaze, akaze, orb, and brisk," in 2018 International conference on computing, mathematics and engineering technologies (iCoMET), pp. 1–10, IEEE, 2018.

[36] P. Kulkarni, A. Magikar, and T. Pendse, "A Practical Approach to Camera Calibration for Part Alignment for Hybrid Additive Manufacturing Using Computer Vision," in Intelligent Manufacturing and Energy Sustainability, pp. 221–229, Springer, 2020.

[37] Mitutoyo, "Small Tool Instruments and Reference Gages."

[38] G. Bradski, "The OpenCV Library," Dr. Dobb's Journal of Software Tools, 2000.

[39] N. M. O'Dowd, A. J. Wachtor, and M. D. Todd, "A model for describing phase-converted image intensity noise in digital fringe projection techniques," Optics and Lasers in Engineering, vol. 134, p. 106293, 2020.

[40] N. M. O'Dowd, A. J. Wachtor, and M. D. Todd, "A probability density function model describing height estimation uncertainty due to image pixel intensity noise in digital fringe projection measurements," Optics and Lasers in Engineering, vol. 138, p. 106422, 2021.

[41] G. H. Notni and G. Notni, "Digital fringe projection in 3D shape measurement: an error analysis," in Optical Measurement Systems for Industrial Inspection III, vol. 5144, pp. 372–380, International Society for Optics and Photonics, 2003.